A 28-GHz Harmonic-Tuned Power Amplifier in 130-nm SiGe BiCMOS

Anirban Sarkar, *Student Member, IEEE*, and Brian A. Floyd, *Senior Member, IEEE*

Abstract—The design methodology and measurement results of a millimeter-wave harmonic-tuned power amplifier (PA) are presented. The PA uses optimum fundamental and second-harmonic terminations to achieve high peak power-added efficiency (PAE). We present a parasitic-aware design technique for the output network realized as a bandpass filter cascaded with or surrounded by a low-pass matching network. This technique demonstrates a method of manipulating the second-harmonic phase of a Chebyshev bandpass filter, while maintaining a suitable impedance match at the fundamental. The technique is applied to a 28-GHz PA in SiGe BiCMOS, which achieves 15.3-dB gain, 18.6-dBm saturated output power, 15.5-dBm output 1-dB compression point, and 35.3% peak PAE. When backed off 6- from 1-dB compression, the PA achieves 11.5% PAE with a third-order intermodulation product of −33.7 dBc.

Index Terms—Continuous mode, fifth-generation (5G), harmonic matching network design, millimeter-wave (mm-wave), power amplifier (PA), SiGe.

I. INTRODUCTION

MOBILE millimeter-wave (mm-wave) broadband systems at 28 GHz have the potential to support high-throughput fifth-generation (5G) cellular networks [1]–[3]. Based on link budgets presented in [1] and [2], the handset's up-link transmitter needs moderate beamforming capabilities with a four- to eight-element phased array. Specifically, as shown in [2], the receiver sensitivity (P_R) for a data rate of 0.65 Gb/s is estimated to be −74 dBm.[1] To achieve a 20-dB link margin (LM) at a 200-m distance (D), the effective isotropic radiated power (EIRP) needed at the mobile transmitter's output is about 30 dBm, given by

$$\text{EIRP} = P_R - G_{\text{RX}} + 20\log_{10}\left(\frac{4\pi D}{\lambda}\right) + \text{LM} \qquad (1)$$

where G_{RX} is the antenna gain of the base station receiver, assumed here to be 23 dB (∼100 elements, each with 3-dBi unit antennas). This EIRP can be achieved at the handset using an eight-element phased array ($N = 8$) with 9-dBm output power per element ($P_{\text{el}} = \text{EIRP} - 20\log_{10}(N) - G_{\text{TX}}$) and unit antennas having 3-dBi gain (G_{TX}). Orthogonal frequency-division-multiplexing (OFDM) schemes used

in fourth-generation cellular systems can have 10-dB peak-to-average power ratio (PAPR) for 1024 subcarriers [4], and we assume that 5G systems will be similar. Techniques proposed in [5] can reduce the OFDM waveform PAPR to 6–7 dB at the cost of implementation complexity, bandwidth, and/or bit-error-rate degradation. Assuming a 6-dB backoff for our design, the 1-dB compressed output power ($\text{oP}_{1\text{dB}}$) per element should therefore be > 15 dBm for an eight-element array.[2]

The handset's phased-array transmitter needs to be power efficient to maximize battery life. For example, to limit the eight-element phased-array front-end power consumption to 0.6 W, each transmitter element needs to have greater than 10.7% power-added efficiency (PAE) at 6-dB backoff. Improving the power amplifier (PA) efficiency at power levels ranging from backoff to 1-dB compression point ($P_{1\text{dB}}$) is thus of extreme importance.

Harmonic impedance terminations can be used to improve the PA efficiency through the shaping of the voltage and/or current waveforms at the output of the device. These harmonic terminations are used in high-efficiency PA modes, including Class-B, Class-J, Class-E, and Class-F [6]. A literature survey of mm-wave PAs at Ka-, Q-, and V-bands [7]–[20] reveals that most of these PAs operate in Class-AB mode, with a few Class-E and Class-F designs. With the exception of the Class-F PAs in [17]–[19], little information is found on the design methods for harmonic output-matching networks.

Recently, the continuous Class-B mode has been formalized, wherein a *continuum* of harmonic terminations can be used to provide for high efficiency, high linearity, and broadband operation [6], [21]–[25]. Class-J and Class-B represent points along this continuum, and other points along this continuum can also be used to achieve high performance. The Class-F and F^{-1} modes have also been extended to continuous modes that allow reactive terminations for second and/or third harmonic [21], [26]. However, as in traditional Class-F, we need to operate the PA in saturation and allow the voltage to swing into the knee region to generate a significant third-harmonic component of current or voltage. For our 5G application, operation at backoff and high linearity is essential; hence, we prefer continuous Class-B (or Class-AB).

To the authors' knowledge, a design method for a harmonic output matching network suitable for integrated mm-wave PAs operating along the Class-B/J continuum has not been described. In this paper, we present such a method and adapt

[1]Assumes signal-to-noise ratio of 4.7 dB, receiver noise figure of 5 dB, and 1-GHz receiver bandwidth

[2]The per-element $\text{oP}_{1\text{dB}}$ would increase to 21 dBm for a four-element array.

it to accommodate parasitics of on-chip passive components. We first review the continuous mode in Section II, modified for Class-AB. A harmonic matching network consisting of a Chebyshev bandpass filter cascaded or subsumed within a fundamental-frequency matching network is then presented in Section III. We benchmark our approach in Section IV through a simulation study between classical Class-AB, two-element LC-tuned, and continuous Class-AB PAs. Finally, we validate our approach in Section V through the realization of a fully integrated 28-GHz harmonic-tuned PA in 130-nm GlobalFoundries SiGe BiCMOS 8HP technology which achieves 35.3% peak PAE and 18.6-dBm saturated output power, with 11.5% PAE at 6-dB backoff from a 15.5-dBm oP_{1dB}. This PA was first reported in [27] and classified as Class-J, but as will be shown, the PA is better classified as operating along a Class-AB continuum.

II. CONTINUOUS CLASS-AB POWER AMPLIFIER

The continuous Class-B mode PA was introduced in [21], and refers to the continuum of harmonic terminations, which can be leveraged to achieve wideband operation. In this paper, we focus on the continuous Class-AB mode design, rather than continuous Class-B described in [21], as Class-AB provides higher gain which is useful for silicon mm-wave PAs. The current and voltage waveforms for continuous Class-AB mode can be written in terms of their harmonic components as

$$I(t) = I_{dc} + I_1 \cos(\omega t) + I_2 \cos(2\omega t) + \sum_{r=3}^{\infty} I_r \cos(r\omega t) \quad (2)$$

$$V(t) = V_{dc} - V_1 \left(\cos(\omega t) - \beta \sin(\omega t) + \frac{\beta}{2} \sin(2\omega t) \right) \quad (3)$$

where I_r is the amplitude of the rth harmonic component of current. Fundamental voltage amplitude, V_1, equals $V_{dc} - V_K$, where V_K is the knee voltage of the transistor. By varying the parameter β from -1 to 1, a series of waveforms can be generated which theoretically has the same output power, efficiency, and linearity as the classical Class-AB PA ($\beta = 0$).

The second harmonic current, I_2, is a function of the conduction angle (θ), and can be shown to be [6, Ch. 3, p. 41]

$$I_2 = \frac{4}{3} \frac{\sin^3\left(\frac{\theta}{2}\right)}{(\theta - \sin(\theta))} I_1. \quad (4)$$

Using this relationship, the fundamental-frequency (Z_1) and second-harmonic load impedances (Z_2) are given as

$$Z_1 = R_{opt}(1 + j\beta) \quad (5)$$

$$Z_2 = -j\frac{3}{8} R_{opt} \frac{(\theta - \sin(\theta))}{\sin^3\left(\frac{\theta}{2}\right)} \beta \quad (6)$$

where $R_{opt} = V_1/I_1$ is the optimum fundamental impedance for the classical Class-AB PA.

As evident in (3), the continuous Class-AB mode does result in higher voltage swing at the device; hence, devices with higher breakdown voltage are preferred. The higher voltage swing is handled in SiGe technology through the use of cascode amplifier structures, since these are limited by the
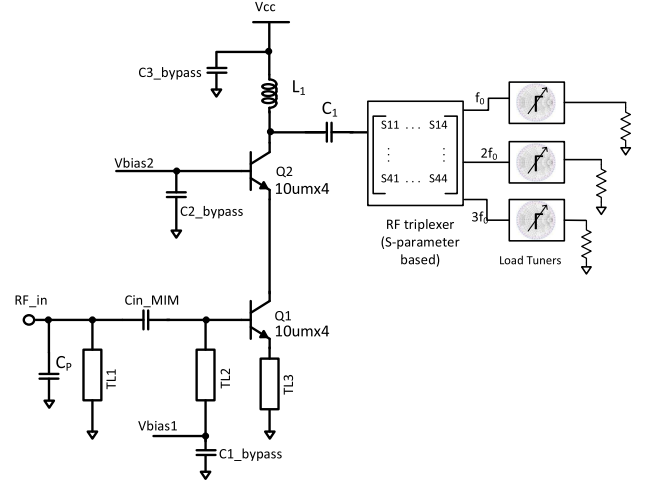

Fig. 1. Schematic of cascode PA with triplexer-based load pull setup.

n-p-n BV_{CBO} (equal to 6 V in SiGe 8HP), rather than BV_{CEO} (equal to 1.8 V in SiGe 8HP).

The cascode PA used in this work is designed to meet the output power requirements for our 28-GHz 5G application. The initial schematic is shown in Fig. 1. To achieve a minimum of 15-dB gain with high efficiency, the cascode amplifier is biased with a current density of 0.5 mA/μm with base voltages of $V_{bias1} = 0.85$ V and $V_{bias2} = 1.7$ V for the bottom (Q_1) and top (Q_2) devices, respectively. The knee voltage V_K for the cascode amplifier is approximately 0.9 V, and the supply voltage is set to 3.6 V. For $\beta = 0$, these set the RF voltage amplitude (V_{RF}) to 2.7 V. With this supply voltage and Q_2 base voltage, the range of β which can be supported without entering breakdown is $|\beta| < 0.67$, corresponding to a peak collector voltage less than 7.7 V and a peak collector-base voltage less than 6 V.

The current amplitude (I_1) is set to be $\sim$37 mA, dictated by a 17-dBm output power target to provide margin over our system requirement. The calculated quiescent current is 19 mA for a 1.25π conduction angle. Based on this, we choose an emitter length of four 10-μm stripes in parallel to achieve quiescent current density of 0.5-mA/μm. With our values of voltage and current amplitudes, the calculated optimum fundamental impedance is $R_{opt} = V_1/I_1 = 72$ Ω. A load-pull simulation of the ideal Class-AB mode ($\beta = 0$) shows that the optimum fundamental impedance for maximum PAE is 65 Ω which is close to the calculated load-line value. With the device size and operating current set, we then impedance match the input using a Π-network topology, shown in Fig. 1.

Although we could use a larger device size to set R_{opt} close to 50 Ω, we choose not to do so for a few reasons. First, the increased capacitance at the PA input and output can reduce bandwidth. Second, for devices with a large number of fingers, unequal current and temperature profiles across the device can degrade performance [28].

Before beginning to design an output matching network that can provide the necessary harmonic impedances described in (5) and (6), we check our network assumption by performing a harmonic load pull within the simulator. This simulation
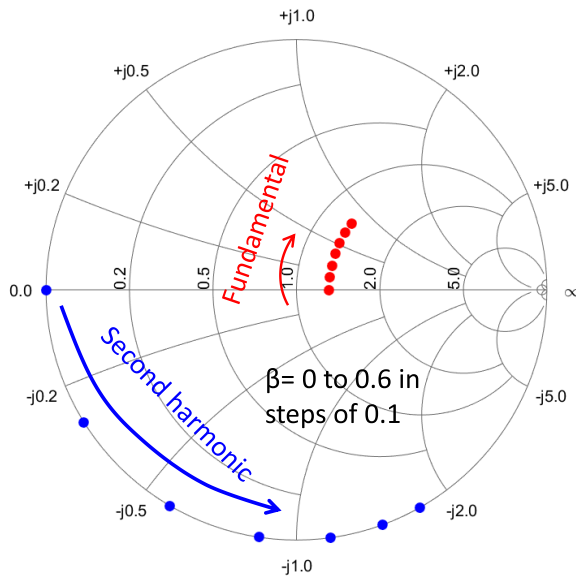
β	oP$_{1dB}$ (dBm)	Peak PAE (%)	PAE @ P$_{1dB}$ (%)
0	17.6	42.2	42
0.1	17.8	44.1	43.8
0.2	18.2	48.7	45.5
0.3	18.6	54.3	47.9
0.4	19	54.6	49.7
0.5	19	53.6	49.8
0.6	19	52.2	49

Fig. 2.   Load-pull simulation with β varied from 0 to 0.6.

Fig. 3.   Load-pull simulation with finite second-harmonic resistance and optimum fundamental impedance from Fig. 2.

will account for the nonlinearities of the device. These non-idealities make it difficult to obtain a full analytic solution for optimum harmonic impedances, as described in [6]. Our simulation uses the HiCUM model for SiGe 8HP. The previous results from the authors have validated the accuracy of the model for fundamental-frequency terminations; however, measurement validation of the second and third harmonics cannot be performed at this time due to equipment limitations.

The harmonic load-pull simulation setup is shown in Fig. 1. A bias-tee connects Q_2's collector to the output through C_1 and to the supply through L_1. An ideal triplexer is implemented as an S-parameter block to subdivide the output power from the cascode into the fundamental, second-, and third-harmonic frequency components. Each of these is parametrically load pulled as follows. The first- and second-harmonic impedances are set according to (5) and (6). The second-harmonic impedance is then locally swept across resistive components for particular points of interest. The third harmonic is simply shorted because simulations show that it has less than a 2% point effect on PAE.

This impedance sweep focuses on the continuous Class-AB mode, whereas our earlier work in [27] explored a wider sweep for the first three harmonics. In this earlier work, the optimum second-harmonic termination in simulation occurred at $-j75\ \Omega$, which we originally classified as a Class-J condition.
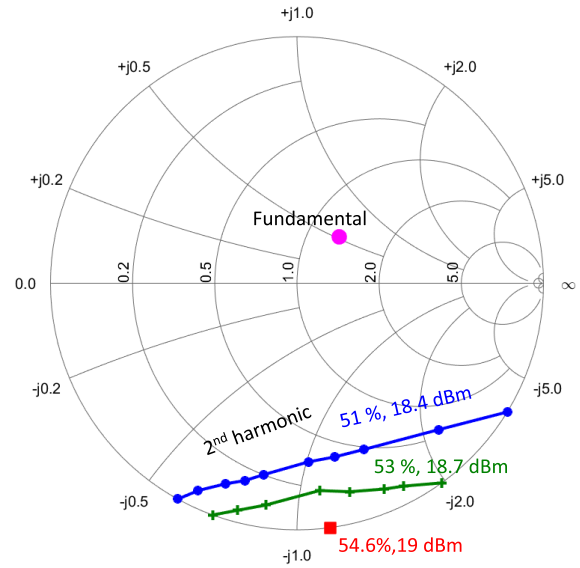
Class-J in this use is generically referred to PAs having a complex fundamental and a reactive second-harmonic termination, according to a definition provided in [6]. However, now with continuous Class-AB mode, we refine our definition such that Class-J refers to fundamental and second-harmonic impedances given by (5) and (6) for $|\beta| = 1$ whereas continuous Class-AB more broadly refers to the full range of possible values of β.

In addition to this terminology update, the HiCUM bipolar transistor model has also been recently updated in the SiGe 8HP design kit, and this new model is used for the simulations herein. The model update indicates that optimum performance occurs near a second-harmonic termination of $-j62.5\ \Omega$.

The results of the harmonic load pull are shown in Fig. 2. These results indicate that the oP$_{1dB}$ and PAE can vary by 2.4 dB and over 12% points with β. According to [29], this is due to three key transistor nonlinearities: 1) the nonlinear input capacitor of Q_1; 2) operation into the knee region; and 3) the nonlinear output capacitor of Q_2. Our results show that the optimum β for maximum PAE is 0.4 which sets a target fundamental impedance of $65 + j25\ \Omega$ and a second-harmonic impedance of $-j62.5\ \Omega$.

To evaluate the impact of a more realistic second-harmonic impedance with a resistive component, we perform a second load pull with the fundamental impedance fixed at $65 + j25\ \Omega$ and vary the resistive and reactive parts of the second harmonic. The results are shown in Fig. 3. While a resistive component in the second-harmonic impedance degrades the PAE and oP$_{1dB}$ as expected, these results indicate that some loss in the second harmonic can be accommodated without significant efficiency degradation. Although the variation of the second-harmonic reactance along these load-pull contours deviates the PA from ideal continuous-mode operation, the effect on linearity is small, according to simulation. We thus target a second-harmonic reactance between $-j60$ and $-j30\ \Omega$ when including the resistance in the second harmonic.
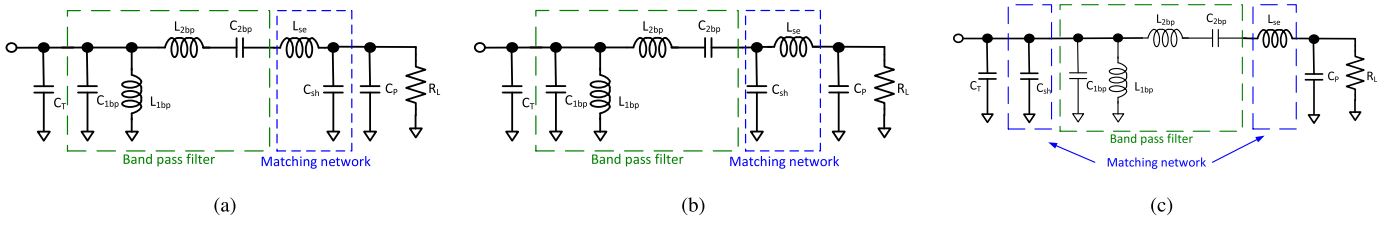
Fig. 4. Network topologies for a cascaded bandpass filter and matching network. (a) Bandpass filter followed by step-down fundamental impedance match. (b) Bandpass filter followed by step-up fundamental impedance match. (c) Bandpass filter subsumed within a step-up fundamental impedance match.

Circuit topologies have been proposed, which can provide a reactive fundamental and a reflective capacitive second harmonic. One such network consists of a series transmission line to set the second-harmonic phase, an open-circuit stub which is a quarter-wavelength at the second harmonic to provide an harmonic short, and then a fundamental-frequency matching network [30]. Although this network is easy to design, the quarter-wave stub can be large and the series transmission line can introduce unwanted insertion loss. We therefore seek to find a harmonic matching network which is both compact and low loss, leading us to consider the topologies presented in the following section.

III. HARMONIC MATCHING NETWORK DESIGN

The primary objective of the harmonic output matching network design is to convert the 50-Ω load to the optimum fundamental and second-harmonic impedances determined by the load-pull analysis. In addition, the network should be able to source the dc bias to the collector of the cascode amplifier and provide dc isolation between the output load and the cascode amplifier. This isolation allows the PA to be later incorporated with transmit/receive switches which may short the output to ground. Our objectives should be met with the lowest possible insertion loss and a compact size. Furthermore, the output network topology should be capable of realizing a wide range of fundamental and second-harmonic impedance so that it is useful for designs having different power specifications or implemented in different technologies.

A general network that is capable of achieving these objectives consists of a bandpass filter, which passes the fundamental and reflects the second harmonic, and a low-pass matching network, which optimally matches the fundamental. The design procedure of the low-pass matching network is straightforward [31]; however, placement of this matching network in relation to the bandpass filter has implications on the overall output network's size and performance. Since the bandpass filter is designed to be transparent at the operating frequency, the fundamental-frequency matching network can either follow [Fig. 4(a) and (b)] or be wrapped around [Fig. 4(c)] the bandpass filter. The location of the low-pass function can be used to reduce the size of the overall network.

The choice of the harmonic network topology in Fig. 4 can be made based on three considerations. First, the configuration of the matching element section can be determined based on whether we need to transform the load to a higher or lower impedance. Second, the ability to combine different elements

including transistor parasitic capacitance, and the pad capacitance can result in a compact and low-loss network. Third, the reference impedance of the bandpass filter is affected by its position with respect to the matching network. The reference impedance of the bandpass filter determines the element values and hence the size and insertion loss of the network.

A. Design of Bandpass Filter for Second-Harmonic

We begin with the design of the bandpass filter to achieve a passband at the fundamental and a full (reactive) reflection with a desired phase at the second harmonic. To achieve a steep out-of-band response, a Chebyshev type-1 filter is proposed. This bandpass filter can be designed such that in-band reflections are minimized and second-harmonic reactance (or phase shift) is specified. The poles and zeros of the reflection coefficient $|\rho|$ of an nth-order Chebyshev type-1 filter can be expressed as [32]

$$Z_{pm} = \begin{cases} \sinh\left[-a + j\frac{\pi}{n}\left(\frac{1}{2} + m\right)\right], & \text{for } n \text{ even} \\ \sinh\left[-a + j\frac{\pi}{n}m\right], & \text{for } n \text{ odd} \end{cases} \quad (7)$$

$$Z_{om} = \begin{cases} \sinh\left[-b + j\frac{\pi}{n}\left(\frac{1}{2} + m\right)\right], & \text{for } n \text{ even} \\ \sinh\left[-b + j\frac{\pi}{n}m\right], & \text{for } n \text{ odd} \end{cases} \quad (8)$$

where m is an integer-valued index varying over the range

$$m = \begin{cases} -\frac{n}{2} \text{ to } \left(\frac{n}{2} - 1\right), & \text{for } n \text{ even} \\ -\left(\frac{n-1}{2}\right) \text{ to } \left(\frac{n-1}{2}\right), & \text{for } n \text{ odd.} \end{cases} \quad (9)$$

Parameters a and b (real numbers ≥ 0, a$\geq$b) determine the magnitude of maximum and minimum reflection coefficient, $|\rho|_{\max}$ and $|\rho|_{min}$, from zero up to the cutoff frequency

$$|\rho|_{\max} = \frac{\cosh(nb)}{\cosh(na)} \quad (10)$$

$$|\rho|_{\min} = \frac{\sinh(nb)}{\sinh(na)}. \quad (11)$$

All poles and zeros of $|\rho|$ are determined by the two independent variables a and b; thus, two conditions are necessary to determine the filter reflection coefficient. In this paper, the two conditions we impose are the minimum $|\rho|_{\max}$ and a specific phase of a large reflection (ideally perfect reflection) at the

second harmonic. The required second-harmonic phase can be obtained by setting

$$
\begin{aligned}
\arg(\rho_{2\text{ndopt}}) &= \sum_m \arg(j\omega_{2nd} - Z_{\text{om}}) - \sum_m \arg(j\omega_{2nd} - Z_{\text{pm}}) \\
&= \sum_m \arctan\left(\frac{\omega_{2nd} - \cosh(b)\sin\left(\frac{\pi}{n}\left(\frac{1}{2}+m\right)\right)}{\sinh(b)\cos\left(\frac{\pi}{n}\left(\frac{1}{2}+m\right)\right)}\right) \\
&\quad - \sum_m \arctan\left(\frac{\omega_{2nd} - \cosh(a)\sin\left(\frac{\pi}{n}\left(\frac{1}{2}+m\right)\right)}{\sinh(a)\cos\left(\frac{\pi}{n}\left(\frac{1}{2}+m\right)\right)}\right)
\end{aligned} \tag{12}
$$

where $\rho_{2\text{ndopt}}$ is the desired optimum reflection coefficient at the second harmonic frequency and m is taken over the range specified in (9). Parameter ω_{2nd} is the low-pass equivalent of the second harmonic frequency which can be found from (13) by setting $\omega_{\text{BP}} = 2\omega_0$

$$
\omega_{\text{LP}} = \frac{\omega_0}{\omega_2 - \omega_1}\left(\frac{\omega_{\text{BP}}}{\omega_0} - \frac{\omega_0}{\omega_{\text{BP}}}\right) \tag{13}
$$

where ω_1 and ω_2 are band-edge frequencies and $\omega_0 = (\omega_1\omega_2)^{1/2}$ is the center frequency of the band.

Maximum in-band reflection coefficient ($|\rho|_{\max}$) can be minimized subject to the constraint in (12) using the method of undetermined multipliers. This is the same procedure used in [32] but for a different set of constraints. Due to the arctangent function involved in (12), it is difficult to derive a minimum $|\rho|_{\max}$ condition for a generalized n-order filter. Here, we derive the condition for minimum $|\rho|_{\max}$ for a second-order filter.

For a second-order filter ($n = 2$, $m = \{-1, 0\}$)

$$
\begin{aligned}
\arg(\rho_{2\text{ndopt}}) &= \arctan\left(\frac{\sqrt{2}\omega_{2nd} - \cosh(b)}{\sinh(b)}\right) \\
&\quad + \arctan\left(\frac{\sqrt{2}\omega_{2nd} + \cosh(b)}{\sinh(b)}\right) \\
&\quad - \arctan\left(\frac{\sqrt{2}\omega_{2nd} - \cosh(a)}{\sinh(a)}\right) \\
&\quad - \arctan\left(\frac{\sqrt{2}\omega_{2nd} + \cosh(a)}{\sinh(a)}\right) = \phi(a, b).
\end{aligned} \tag{14}
$$

Applying the method of undetermined multipliers to minimize $|\rho|_{\max}$ with the constraint in (14) results in the following:

$$
\frac{\partial \phi(a, b)}{\partial a} - \lambda \frac{\partial \phi(a, b)}{\partial b} = 0 \tag{15}
$$

$$
\frac{\partial |\rho|_{\max}}{\partial a} - \lambda \frac{\partial |\rho|_{\max}}{\partial b} = 0. \tag{16}
$$

After evaluating the derivatives (15) can be written as

$$
-f(a) - \lambda f(b) = 0 \tag{17}
$$

where

$$
f(x) = \frac{1 - \sqrt{2}\omega_{2nd}\cosh(x)}{\sinh^2(x) + (\sqrt{2}\omega_{2nd} - \cosh(x))^2} - \frac{1 + \sqrt{2}\omega_{2nd}\cosh(x)}{\sinh^2(x) + (\sqrt{2}\omega_{2nd} + \cosh(x))^2} \tag{18}
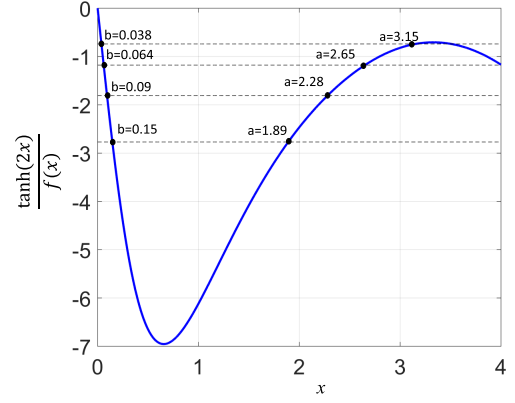$$

Fig. 5.   Plot of $((\tanh(2x))/(f(x)))$ and graphical solutions of (20).
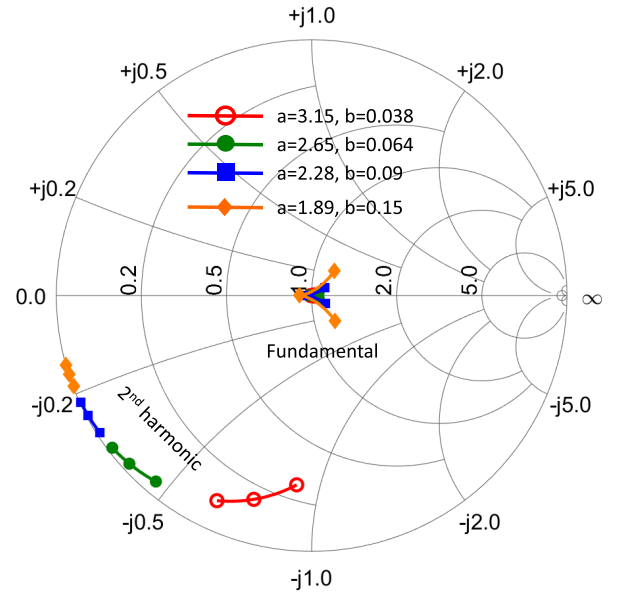

Fig. 6.   Reflection coefficient of a second-order bandpass filter demonstrating second-harmonic phase tuning and well-matched fundamental. Frequency range corresponds to 26–30 GHz for fundamental and 52–60 GHz for second harmonic.

and (16) can be written as

$$
-\frac{\cosh(2b)\cdot 2\sinh(2a)}{\cosh^2(2a)} - \lambda\frac{2\sinh(2b)}{\cosh(2a)} = 0. \tag{19}
$$

Eliminating λ from (17) and (19), we obtain

$$
\frac{\tanh(2a)}{f(a)} = \frac{\tanh(2b)}{f(b)}. \tag{20}
$$

Solutions to (20) can be obtained graphically as shown in Fig. 5, and these values of a and b can be substituted into (14) to obtain the phase condition. Fig. 6 shows the reflection coefficient looking into the bandpass filter at both the fundamental and second-harmonic, for a range of valid a and b. These results indicate that the phase can be tuned by $55°$, while maintaining an in-band reflection coefficient less than -25 dB and a second-harmonic reflection coefficient higher than -1.7 dB across 26.5–29.5 GHz.
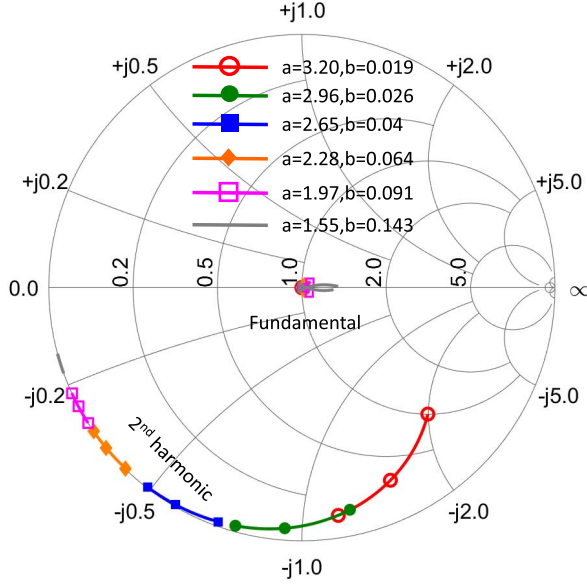
Fig. 7. Reflection coefficient of a third-order bandpass filter demonstrating second-harmonic phase tuning and well-matched fundamental. Frequency range corresponds to 26–30 GHz for fundamental and 52–60 GHz for second harmonic.

The second-harmonic reflection coefficient magnitude can be improved further by using a third-order filter. If we define

$$g(x) = \frac{\sqrt{3} - 2\omega_{\text{2nd}}\cosh(b)}{\sinh^2(x) + (2\omega_{\text{2nd}} - \sqrt{3}\cosh(b))^2}$$
$$- \frac{\sqrt{3} + 2\omega_{\text{2nd}}\cosh(b)}{\sinh^2(x) + (2\omega_{\text{2nd}} + \sqrt{3}\cosh(b))^2}$$
$$- \frac{\omega_{2nd}\cosh(x)}{\omega_{2nd}^2 + \sinh^2(x)} \tag{21}$$

then minimum $|\rho|_{\max}$ condition for the third-order filter is similar to (20) and can be written as

$$\frac{\tanh(3a)}{g(a)} = \frac{\tanh(3b)}{g(b)}. \tag{22}$$

The reflection coefficient for the third-order filter is shown in Fig. 7. The third-order filter also shows an improved second-harmonic phase tuning capability of 100°.

After the values of a and b have been determined for the required second-harmonic phase, the poles and zeros of ρ are known. The remaining steps in the design of the bandpass filter are: 1) express ρ as a rational function in the s-domain; 2) extract the LC low-pass ladder network; and 3) perform low-pass to bandpass and then impedance transformations. These steps are standard for bandpass filter design [31], [33] and are demonstrated in the following section. Note that a negative sign was used for the reflection coefficients for plots in Figs. 6 and 7, meaning the first element is a parallel LC resonator.

Finally, when the fundamental-frequency matching network is wrapped around the bandpass filter [Fig. 4(c)], the target second-harmonic phase of the bandpass filter should be revised by taking into account the phase shift of the

fundamental-frequency matching component. This can be done by de-embedding that impedance.

B. Design Examples

Examples of two harmonic matching network designs are shown in Fig. 8, for fundamental matching networks either following or wrapped around the bandpass filter. The target fundamental and second-harmonic impedances are taken from our original design, namely, $Z_1 = 65 + j25\ \Omega$ (equivalent to $74.6 || j194\ \Omega$) and $Z_2 = -j40\ \Omega$ (taking into account the impact of loss at the second harmonic, as in Fig. 3). The network topologies of Fig. 4(b) or (c) are selected for this example because R_L needs to be transformed to a higher impedance. In these examples, passive losses and parasitics are not yet taken into account, but will be included subsequently.

We begin with the topology from Fig. 4(b) and shown again in Fig. 8(a), where the load impedance is first transformed into the target fundamental impedance and then the bandpass filter is designed. A series inductor, $L_{\text{se}} = 200$ pH, and shunt capacitor, $C_{\text{sh}} = 25$ fF, transform the 50-Ω load into $65 + j25\ \Omega$ at the fundamental. The bandpass filter is then designed with a reference impedance of 74.6 Ω, which is the real part of the parallel equivalent of Z_1. For this reference impedance, the required second-harmonic impedance corresponds to a phase of $\arg(\rho_{\text{2ndopt}}) = 123°$. A second-order low-pass Chebyshev prototype with 123° second-harmonic phase shift is achieved with $a = 2.94$ and $b = 0.044$. The low-pass prototype elements are $C_{\text{shunt}} = 0.151$ F and $L_{\text{series}} = 0.148$ H and the bandpass filter elements are $C_{1bp} = 107$ fF, $L_{1bp} = 300$ pH, $C_{2bp} = 55$ fF, and $L_{2bp} = 584$ pH. The final network and its simulated reflection coefficient are shown in Fig. 8(a).

We now design a harmonic matching network where the fundamental impedance matching network is wrapped around the bandpass filter—the topology from Fig. 4(c) and shown again in Fig. 8(b). Since the final series leg now includes two inductors and a single capacitor, these can be simplified into a single series LC network. As a result, this topology is preferred over the previous for smaller chip size. The values necessary for the fundamental match remain the same; however, we must now absorb the shunt capacitance into the design of the bandpass filter. The rotation of the second-harmonic impedance due to C_{sh} is de-embedded by modifying the second-harmonic impedance target of the bandpass filter to $-j62\ \Omega$. The reference impedance for the filter is still 74.6 Ω. The required second-harmonic impedance corresponds to a phase of $\arg(\rho_{\text{2ndopt}}) = 100°$. A second-order low-pass Chebyshev prototype with 100° second-harmonic phase shift is achieved with $a = 3.2$ and $b = 0.037$. The low-pass prototype elements are $C_{\text{shunt}} = 0.116$ F and $L_{\text{series}} = 0.114$ H and the bandpass filter elements are $C_{1bp} = 82$ fF, $L_{1bp} = 393$ pH, $C_{2bp} = 72$ fF, and $L_{2bp} = 453$ pH. The final network and its simulated reflection coefficient are shown in Fig. 8(b).

C. Compensation of Network for Finite-Q Elements

Passive component losses deviate ρ from the optimum value and must be compensated for within the design. The procedure
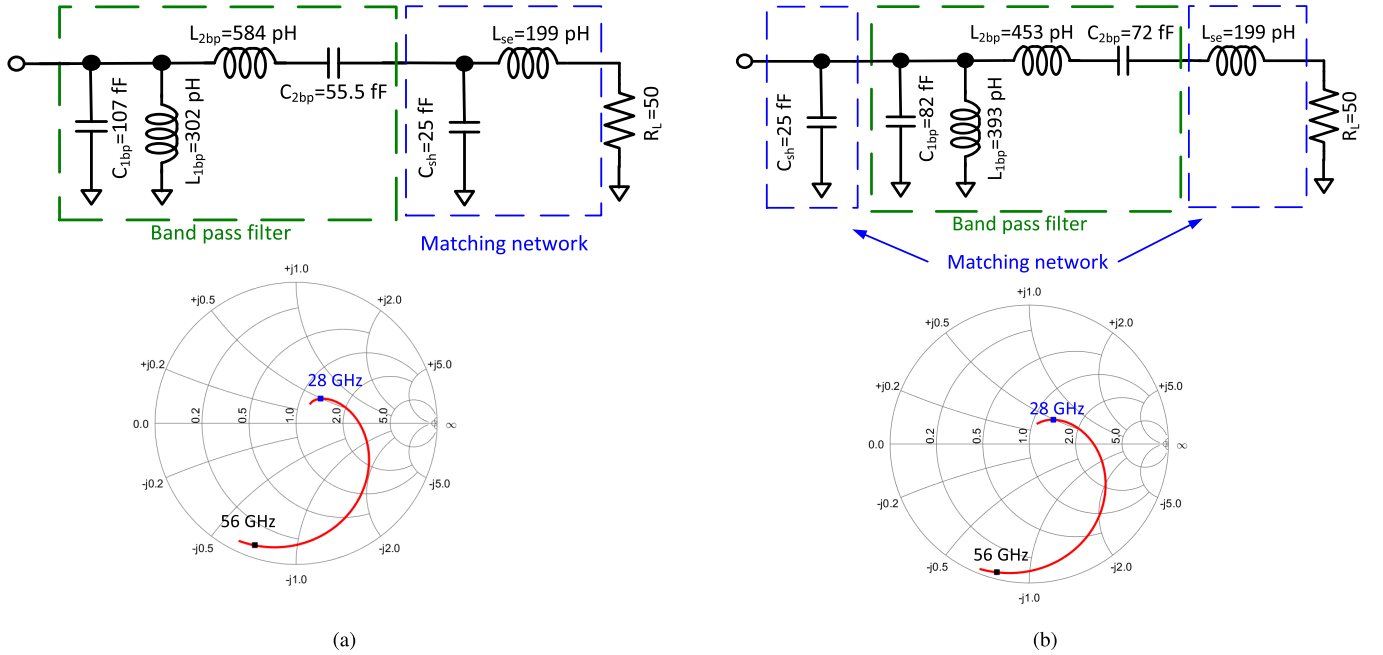
Fig. 8. Design examples for harmonic matching network topologies for PA targeting $Z_1 = 65 + j25 \ \Omega$ and $Z_2 = -j40 \ \Omega$. (a) Example from Fig. 4(b) where the matching network follows the bandpass filter. (b) Example from Fig. 4(c) where the matching network is wrapped around the bandpass filter.

for compensation of passive losses within the bandpass filter can be explained better if we consider one of the networks, namely Fig. 8(b).

First, the loss of the series tank (L_{2bp} and C_{2bp}) can be compensated by simply modifying the matching network on the right side by adjusting the target load impedance. Second, the resistance r_P of the parallel tank (L_{1bp} and C_{1bp}) shunts the reference impedance of the filter R_0. Thus, the effect of r_P can be compensated by increasing the filter reference impedance to R_0' such that $r_P || R_0' = R_0$, where R_0 is the original reference impedance. This can be incorporated in the design procedure described above when we transform the low-pass filter with 1-Ω reference impedance to a bandpass filter of a desired reference impedance. For example, if the shunt capacitor of the low-pass network is C, the bandpass filter elements can be determined as $L_{1bp} = (R_0'/(\alpha C \omega_0))$ and $C_{1bp} = (\alpha C/(\omega_0 R_0'))$, where $\alpha = (\omega_0/(\omega_2 - \omega_1))$ [31], [33]. The modified reference impedance R_0' can be related to the original reference impedance by

$$R_0' = R_0 \frac{Q_{L1} Q_{C1} + \alpha C(Q_{L1} + Q_{C1})}{Q_{L1} Q_{C1}} \qquad (23)$$

where Q_{L1} and Q_{C1} are unloaded quality-factors of L_{1bp} and C_{1bp}. Equation (23) indicates that the modified reference impedance would always be greater for finite quality passives than that for ideal passives. It is difficult to estimate the exact R_0' because Q_{L1} and Q_{C1} are functions of L_{1bp} and C_{1bp}; however, an approximate estimation of R_0' can be made using average values of Q_{L1} and Q_{C1} suitable for the technology. Furthermore, an iterative approach can be taken, where the network is first designed for loss-less components, then these L and C values are used to estimate Q factors, which then are

used to update the reference impedance. Iteration can continue until we converge on accurate Q values.

D. Final Network Accommodating Parasitics

We conclude this section by discussing how the final design is updated to accommodate parasitic shunt capacitance and interconnect inductance. We also discuss how the design values can be adjusted to reduce insertion loss. This example is done for the network in Fig. 8(b) and describes the final design values used for the PA we have implemented and which is discussed in Section V.

First, the network is updated to accommodate parasitics and the pad capacitor. We update the low-pass prototype and the fundamental match with a new load impedance ($R_L || C_P$), where C_P (46 fF) is the pad capacitance which shunts the output load. The filter's reference impedance was originally R_{optFP} (74.6 Ω) for a loss-less network; however, assuming Q-factors of 25 and 14 for the inductor and capacitors and band-edge frequencies of 26.5 and 29.5 GHz, the impedance is increased to 84 Ω according to (23). The values of the fundamental network and bandpass filter elements are now $C_{\text{sh}} = 30$ fF, $L_{\text{se}} = 330$ pH, $C_{1bp} = 77$ fF, $L_{1bp} = 421$ pH, $C_{2bp} = 61$ fF, and $L_{2bp} = 536$ pH. Also, instead of using an extra inductance to implement L_{se}, C_{2bp} is increased to 157 fF.

The series capacitor C_{2bp} and inductor L_{2bp} can have undesirable insertion loss at 28 GHz. Also, the resonant frequency of the inductor L_{2bp}, realized here as a 1.25-turn spiral, is 40 GHz, which is close to our frequency of operation. The fundamental match can be maintained if the inductor L_{2bp} is reduced and the capacitor C_{2bp} is increased such that the impedance of the series tank at fundamental $Z_{\text{series}} = j(\omega L_{2bp} - (1/\omega C_{2bp}))$ remains constant. The impact on the
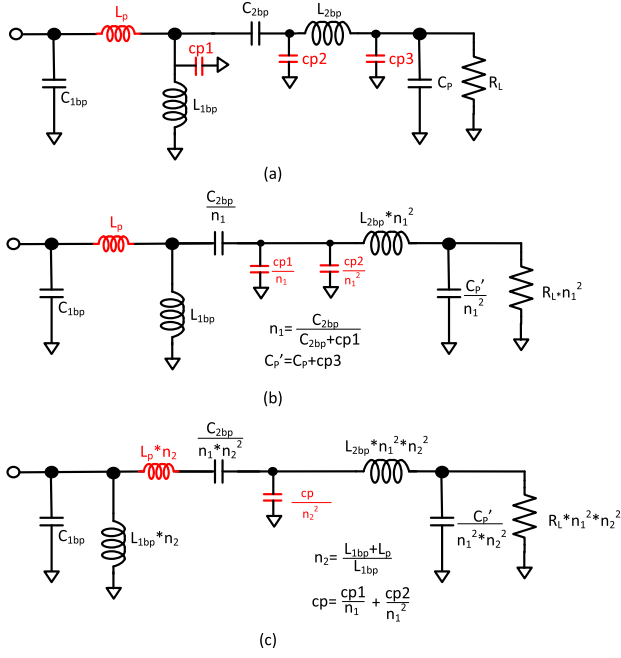
Fig. 9. Effect of parasitic components on the output network. (a) Major parasitic components. (b) Rearrangement of C_{2bp} and $cp1$. (c) Rearrangement of L_{1bp} and L_p.

Fig. 10. Fundamental and second-harmonic impedance of the final network including all parasitics.

(a) Class-AB   (b) LC tuned   (c) Continuous Class-AB

Fig. 11. Output network schematic of PA modes compared in Section IV (top), fundamental and second-harmonic impedances realized by the three networks. (a) Class-AB (green). (b) LC tuned (blue). (c) Continuous mode class-AB (red).

second-harmonic impedance is small as long as the impedance of the series arm is high at the second harmonic. Reducing L_{2bp} to 400 pH and increasing C_{2bp} to 600 fF maintain the fundamental impedance, reduce the insertion loss at fundamental frequency by 0.6 dB, and change the magnitude and phase of the second-harmonic reflection coefficient by 0.5 dB and 4° only.

The last design step is to compensate for the parasitic elements needed to realize an actual design. These parasitics are shown in Fig. 9(a) in red, and are described as follows: C_{1bp} is realized by the device and wiring capacitance; L_p (25 pH) represents the parasitic transmission line between the device and inductor L_{1bp}; $cp1$ (18 fF) is the parasitic capacitance of inductor L_{1bp}; and $cp2$ and $cp3$ (20 fF each) are the parasitic capacitances of inductor L_{2bp}.

Compensation for $cp3$ is straightforward through combining it with the output pad capacitance. To compensate for the other parasitic elements, we perform two Norton transformations as shown in Fig. 9(b) and (c). In Fig. 9(b), a Norton transform was applied to rearrange $cp1$ and C_{2bp} which results in multiplication of all resistance and reactances to the right of C_{2bp} by n_1^2, where $n_1 = ((C_{2bp})/(C_{2bp} + cp1))$. Inductors L_P and L_{1bp} can be rearranged as shown in Fig. 9(c) by using another Norton transform which results in multiplication of all resistance and reactances to the right of L_{1bp} by n_2^2, where $n_2 = ((L_{1bp} + L_p)/(L_{1bp}))$. The network in Fig. 9(c) differs from the original architecture in Fig. 4(c) due to the parasitic capacitor $((cp)/(n_2^2))$ only. The effect of the parasitic capacitor $((cp)/(n_2^2))$ in Fig. 9(a) is to reduce the value of C_{1bp}.

Note that the parasitic elements $cp1$, $cp2$, and $cp3$ are dependent on the values of the passive elements L_{1bp} and L_{2bp}. The final values of the network components were $C_{1bp} = 85$ fF, $L_{1bp} = 350$ pH, $C_{2bp} = 646$ fF, and
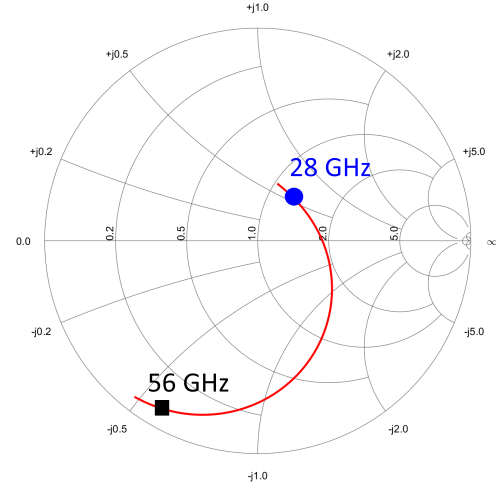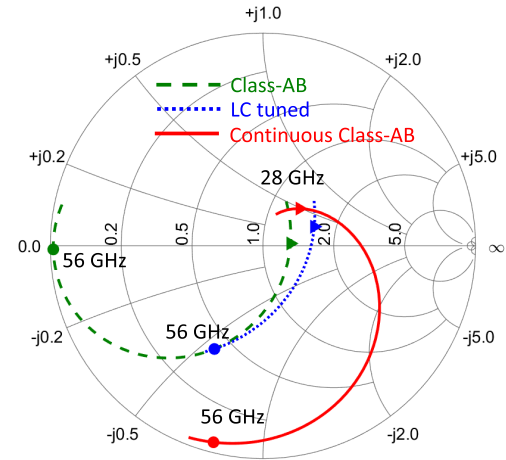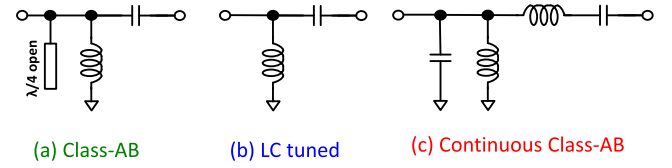
$L_{2bp} = 368$ pH. As illustrated in Fig. 10, the fundamental impedance is the same as the targeted value, whereas the second harmonic impedance was $4 - j32$ Ω compared with a target of $-j40$ Ω.

IV. CLASS-AB PA COMPARISONS

To evaluate the efficacy of harmonic tuning, we compare the continuous Class-AB PA ($\beta = 0.4$) with a classical Class-AB PA ($\beta = 0$) and a simple LC-tuned PA for realistic component loss. The output networks of the three PAs being compared along with the fundamental and second-harmonic impedances are shown in Fig. 11. All PAs have the same operating point and bias conditions as originally presented in Fig. 1.

The classical Class-AB PA shown in Fig. 11(a) is designed using an open-circuited stub which is $\lambda/4$ at the second
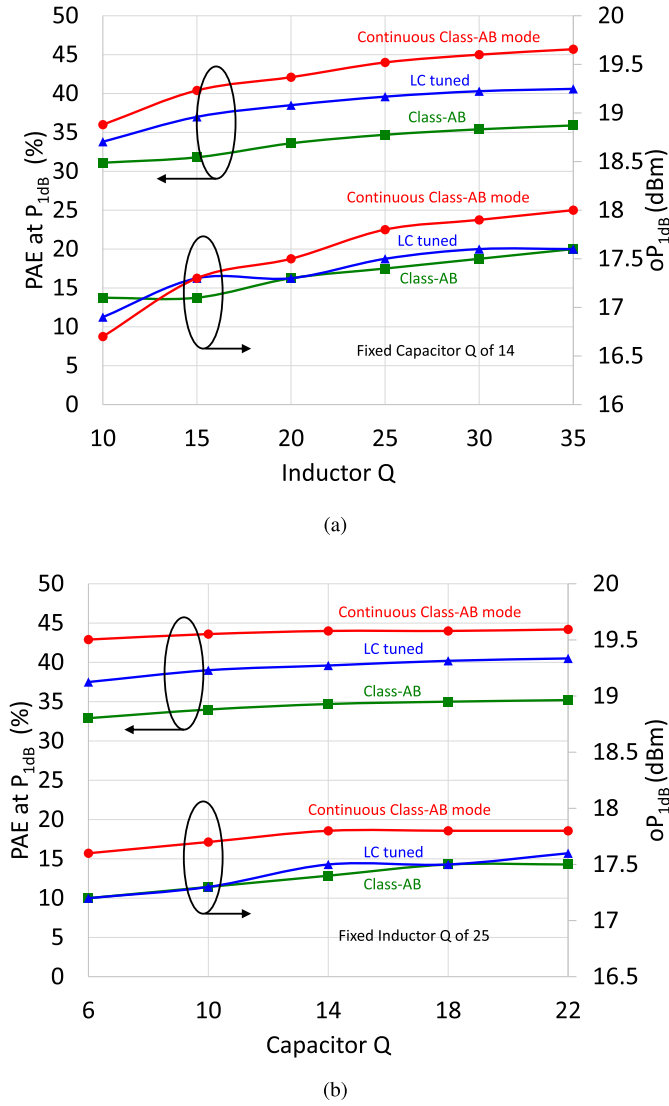
Fig. 12. Effect of finite quality factor of passive elements on 1-dB compression PAE and output power for the three types of Class-AB PA for (a) varying inductor Q with capacitor Q fixed at 14 and (b) varying capacitor Q with inductor Q fixed at 25.

harmonic, where λ is the wavelength. This achieves a second-harmonic short condition. A third-harmonic short could be achieved using another resonant open stub but it is avoided here to reduce the insertion loss of the network. The classical Class-AB network then has a two-element LC network to achieve a fundamental impedance of 65 Ω. The LC-tuned network shown in Fig. 11(b) is initially designed to achieve a fundamental impedance which is the same as the classical Class-AB PA. Then the component values are swept over a limited range to maximize the PAE. Finally, the continuous Class-AB PA shown in Fig. 11(c) uses the network architecture in Fig. 4(c) and the design technique outlined in Section III-B.

Using large-signal PA simulations, the output power and PAE at 1-dB compression is compared for the three PA modes with varying quality factor of inductors and capacitors, as shown in Fig. 12. This shows how much the performance improvement depends upon quality factor. Fig. 12(a) shows the comparison between the PA modes for a fixed capacitor

TABLE I
PERFORMANCE COMPARISON OF PA CLASSES

Ideal Passives			
Class	Class-AB	LC-tuned	Cont. Mode
Gain (dB)	15.7	16.7	17.2
3-dB bandwidth (GHz)	25-31.7	24.3-36.4	25.2-39
P_{sat} (dBm)	18.4	19.8	19.4
oP_{1dB} (dBm)	17.6	17.7	18
Peak PAE (%)	41.1	48.6	53.7
PAE 1-dB comp. (%)	40.6	47.3	52.9
PAE 6-dB-back-off (%)	19.5	20.5	20.7
Finite-Q passives			
Class	Class-AB	LC-tuned	Cont. Mode
Output network loss (dB)	0.5	0.4	0.34
Gain (dB)	14.6	15.4	15.8
3-dB bandwidth (GHz)	24.7-33.4	24-38	25.4-41
P_{sat} (dBm)	18.1	19.4	19
oP_{1dB} (dBm)	17.4	17.5	17.8
Peak PAE (%)	34.7	41	45
PAE 1-dB comp. (%)	34.7	39.6	44
PAE 3-dB-back-off (%)	25.8	28	29.2
PAE 6-dB-back-off (%)	16.6	17.9	18.9
AM-PM 3-dB-back-off (°)	0.1	0.6	3
IM3 3-dB-back-off (dBc)	-54.6	-49	-42.5

quality of 14 with inductor Q varied from 10 to 20. The continuous Class-AB PA shows significant benefit in PAE over the other two modes for inductor Q factors above 15. Similarly, Fig. 12(b) shows the comparison between the PA modes for a fixed inductor Q of 25 with capacitor Q varied from 6 to 22. The capacitor Q degrades the performances of all the PA modes by a similar amount, meaning the benefit of the continuous mode is retained even for low capacitor Q.

A comparison of the PA modes is presented in Table I for ideal passives and for finite-quality passives. For the finite Q factor case, we assume an inductor Q of 25, a capacitor Q of 14, and a transmission line loss of 0.1 dB/mm. The continuous Class-AB mode shows 4%–5% (10%–11%) point benefit in peak PAE and 1-dB compression PAE over the LC-tuned PA (Class-AB PA). The benefit reduces to 1% (3%) point at both 3- and 6-dB backoffs with respect to the LC-tuned PA (Class-AB PA). The continuous Class-AB mode also has a higher gain, a wider 3-dB bandwidth, and a higher oP_{1dB}. A small part of the peak efficiency benefit shown by the continuous Class-AB mode is due to the 0.06-dB (0.16-dB) lower insertion loss of the output network compared with the LC-tuned PA (Class-AB PA). However, by increasing the Q of the passives and equalizing the network losses, we have verified that the continuous Class-AB PA retains 3.6% (9%) point benefit at peak and 1-dB compression point and 0.5%–1% (1.5%–2%) point benefit up to 6-dB backoff over the LC-tuned (Class-AB) PA.
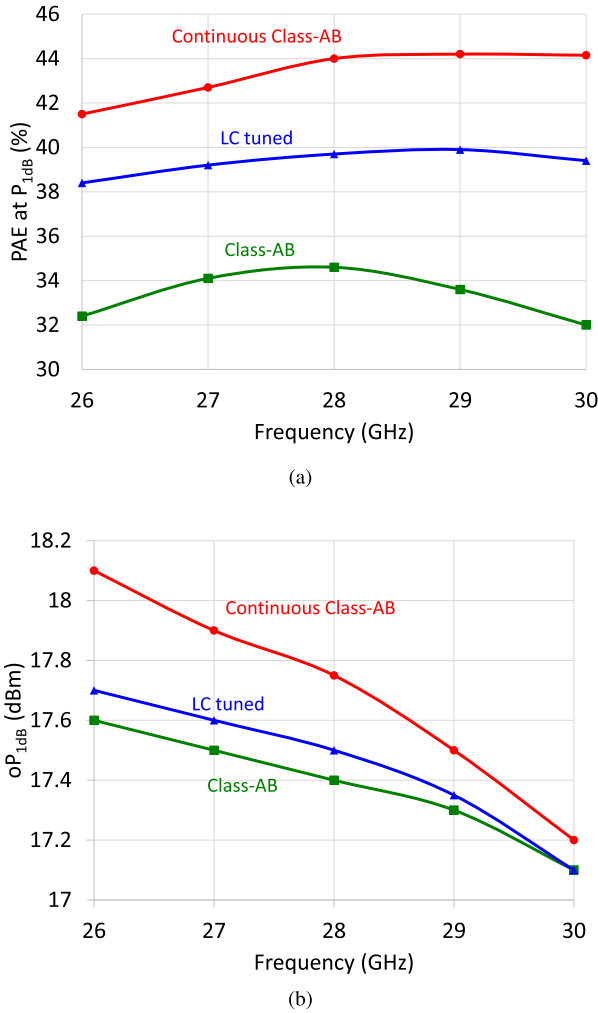
(a)

(b)

Fig. 13. Variation of performance across frequency for classical Class-AB, *LC*-tuned, and continuous Class-AB PAs for (a) PAE and (b) oP$_{1dB}$.

Fig. 14. Schematic of final 28-GHz single-stage PA.
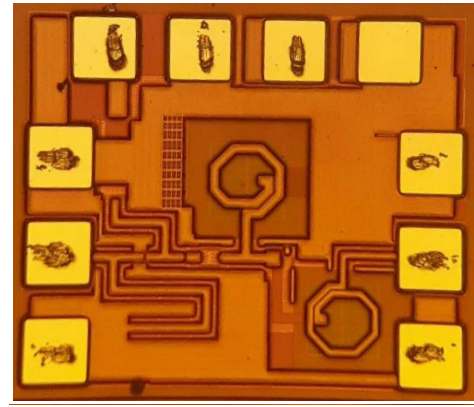
Fig. 15. Die photograph of 28-GHz single-stage PA.

It can be seen that the performance benefit of the continuous Class-AB mode PA over the Class-AB PA is more pronounced near 1-dB compression compared with backed-off power levels. This is due to two nonlinear effects, viz., the collector current–voltage (I–V) knee and the nonlinear collector capacitor, which reduce the overlap between the current and voltage waveforms and improve the power factor between the fundamental current and voltage components in continuous-mode operation. A more detailed explanation is provided in the Appendix.

Linearity of the PA modes can be assessed in simulation from the oP$_{1dB}$, amplitude-modulation to phase-modulation (AM–PM) distortion, and third-order intermodulation distortion product (IM3). The classical Class-AB PA has superior AM–PM and IM3 metrics compared with the other two modes. The continuous Class-AB mode PA has better oP$_{1dB}$ response compared with the *LC*-tuned PA but worse AM–PM and IM3 performance. This can be attributed to the higher output voltage swing of the continuous Class-AB mode which causes a larger variation of the nonlinear device capacitance. However, the IM3 performance of the continuous Class-AB mode is still
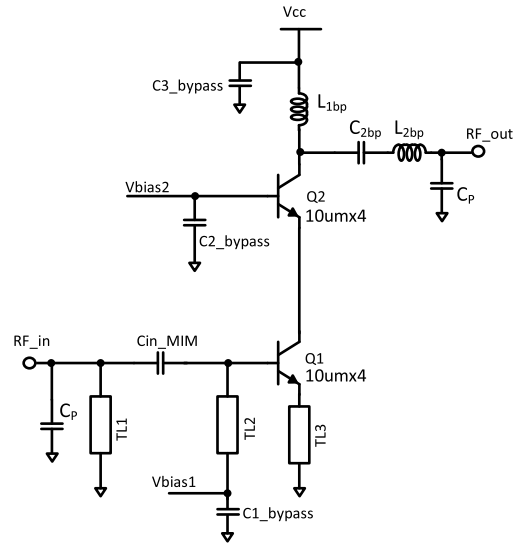
adequate to meet our IM3 target of −33 dBc at 6-dB backoff.

Variation of peak PAE and oP$_{1dB}$ of the three PAs with frequency are shown in Fig. 13. Across 26–30 GHz, the continuous Class-AB mode PA has better PAE and oP$_{1dB}$ than the other two PAs; however, it does show slightly higher variation in oP$_{1dB}$ across the band.

V. IC IMPLEMENTATION AND MEASUREMENTS

To illustrate the performance possible for a continuous Class-AB design in SiGe, we have implemented a 28-GHz PA with a harmonic output harmonic matching network using the topology in Fig. 4(c). The PA was designed and fabricated in 130-nm GlobalFoundries SiGe BiCMOS 8HP technology. The high-performance n-p-n transistor with peak f_T (f_{max}) of 200 GHz (265 GHz) is used because of its superior RF performance. We use a five-layer back-end-of-line, where the top three thick layers (MQ, LY, and AM) are used to realize low-loss passive structures.

The final PA schematic is shown in Fig. 14. The output matching network includes the final component values and transformations we applied from Fig. 9(c). We use a dual-base-collector-base-emitter-base-collector (CBEBC) layout for each device of the cascode. Compared with the CBE style
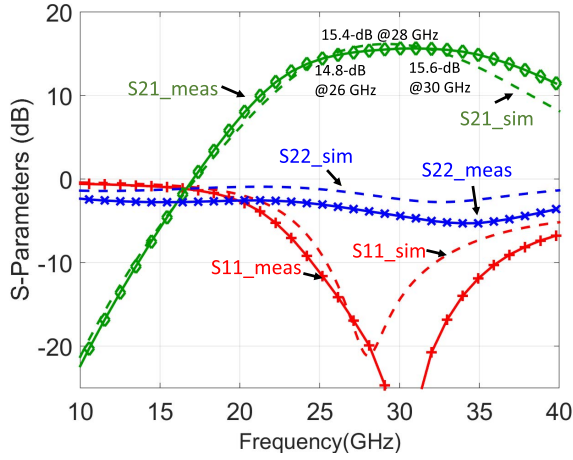
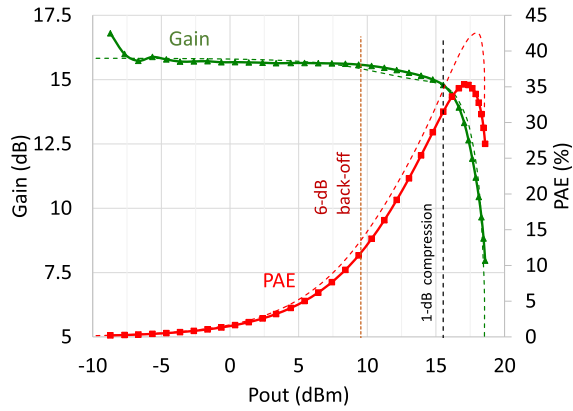Fig. 16.   S-parameter measurement results of the PA.

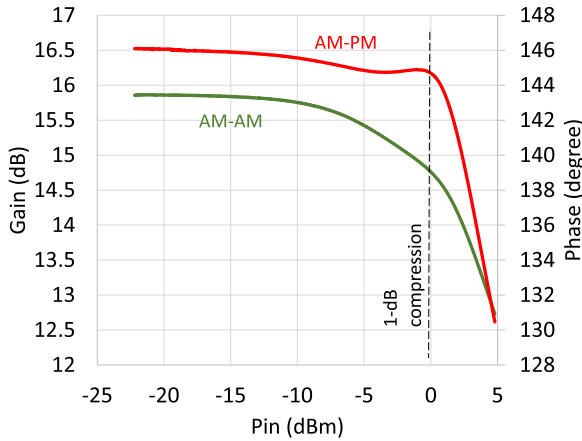Fig. 17.   Swept power measurement results of the PA at 28 GHz (simulation results are shown with dashed curves).

Fig. 18.   AM–PM distortion measurement of the PA at 28 GHz.

Fig. 19.   IM3 distortion measurement of the PA at 28 GHz.

TABLE II
PERFORMANCE OF THE PA ACROSS BAND

Frequency (GHz)	27	28	29
Gain (dB)	15	15.3	15.5
P_{sat} (dBm)	18.8	18.6	18
oP_{1dB} (dBm)	15.1	15.5	15.9
Peak PAE (%)	33.8	35.3	34.7
PAE 1-dB comp. (%)	27.6	31.5	33.2
PAE 6-dB-back-off (%)	10.7	11.5	13.5

TABLE III
MEASURED PA PERFORMANCE VERSUS TEMPERATURE AT 28 GHz

Temperature (°C)	25	56	86
Gain (dB)	15.3	14.3	13.5
P_{sat} (dBm)	18.6	18.3	17
oP_{1dB} (dBm)	15.5	14.4	11.3
Peak PAE (%)	35.3	34	30.6
PAE 1-dB comp. (%)	31.5	27	17.3
PAE 6-dB-back-off (%)	11.5	11.2	8

layout, the CBEBC configuration has higher f_T, f_{max} and lower external base resistance and collector resistance [34], and hence it gives a higher gain and oP_{1dB}. The CBE configuration reduces the emitter inductance as mentioned in [35], however, in our design this is not a problem because we use explicit inductive degeneration at the emitter (TL3) to improve the stability and the linearity of the PA. The four fingers of the device share adjacent deep trench regions for a compa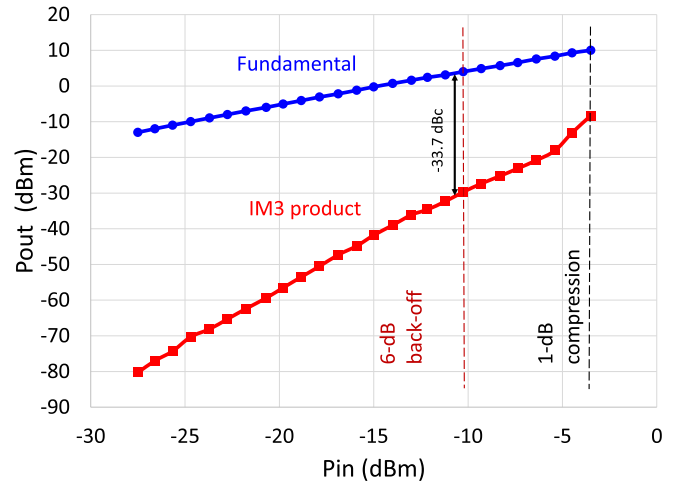ct layout, minimizing device interconnects. The base terminals are wired using M1, M2 metal layers, whereas the emitter and collector terminals are wired using M1, M2, and MQ to meet electromigration current density at 100 °C and to minimize interconnect resistance. Inductors L_{1bp} (octagon, 116-μm diameter, 12-μm width, 1.25 turns) and L_{2bp} (octagon, 110-μm diameter, 8-μm width, 1.25 turns) were implemented in top-level metal with a patterned ground shield in the bottom metal layer. Transmission lines for the input match were implemented as grounded coplanar waveguide. The chip micrograph is shown in Fig. 15, and the die area is 0.61 mm × 0.73 mm, including pads.

The PA measurements were performed with a collector supply voltage of 3.6 V and a collector bias current of 17 mA. S-parameter simulation and measurement results of the PA are shown in Fig. 16. The input match, S_{11}, shows close agreement with the simulations, whereas S_{22} is slightly offset due to an imperfect pad model. The gain at 28 GHz is

TABLE IV
PERFORMANCE COMPARISON WITH Ka AND Q-BAND POWER AMPLIFIERS

Reference	Frequency (GHz)	Architecture	Gain (dB)	Psat (dBm)	oP_{1dB} (dBm)	Peak PAE (%)	PAE at 6-dB-back-off(%)	Technology
This work	**27-29**	**Continuous Class-AB**	**15-15.5**	**18.8-18**	**15.1-15.9**	**33.8-35.3**	**10.7-13.5**	**130-nm SiGe**
[18] Mortazavi	27-31	Class-F	21.2	17.1	15	42	18.5[*]	130-nm SiGe
[17] Mortazavi	26-30	Class-F^{-1}/F	10.3	17.1	15	40	12[*]	130-nm SiGe
[19] Mortazavi	38	Class-F^{-1}	16	16.5	15	38.5	16.5[*]	130-nm SiGe
[9] Datta	39-47	Stacked Class-E	4	23.4	N.A[†]	34.9	N.A[†]	130-nm SiGe
[8] Agah	45	Stacked Class-AB	9.5	18.6	17.5	34.4	15[*]	45-nm SOI CMOS
[15] Dabag	38-47	Stacked	9.4	15.9	N.A[*]	32.7	N.A	45-nm SOI CMOS
[12] Datta	42-46	Class-E, 2-stage	10	20.2	N.A[†]	31.5	N.A[†]	130-nm SiGe
[16] Kim	45	2-stage Class-AB	19.5	15	14.5[*]	27.5	9[*]	45-nm SOI CMOS
[13] Tai	45	Class-B, 2-stage	16.6	17.5	N.A[†]	26	N.A[†]	130-nm SiGe
[14] Chakrabarti	47.5	Stacked Class-EE	9.8	17.9	14[*]	25.5	7.5[*]	45-nm SOI CMOS
[7] Agah	42	Doherty	7	18	11[*]	23	8[*]	45-nm SOI CMOS
[11] Chen	37	2-stacked cascode	8	14.8	11.5	16.2	4.5[*]	45-nm SOI CMOS
[10] Kalantari	42-50	Class-E, Wilkinson combined	6	19.4	16.4	14.4	5[*]	130-nm SiGe
[20] Essing	27	8-way combined, Class-AB	20.7	31	N.A	13	N.A	250-nm SiGe
[37]Tai	42.5-49	16-way combined	18.5	28.4	N.A	10	N.A	130-nm SiGe
[38] Bhat	33-46	8-way combined, Class-E	19.4	27.2	21	10.7	2[*]	45-nm SOI CMOS
[39] Datta	42-47	Class-E, Digitally controlled	13	28.9	N.A	18.4	N.A	130-nm SiGe
[40] Chakrabarti	33-48	Class-E, 2-stacked	13	17.6	13[*]	34.6	8[*]	45-nm SOI CMOS

[*] Estimated from swept power plots. [†] Could not be estimated due to excessive gain expansion

15.3 dB, agreeing with the simulated value. The gain has less than 0.8-dB variation across 26–30 GHz.

Fig. 17 presents measured and simulated gain and PAE versus output power at 28 GHz. The saturated output power (P_{sat}) is 18.6 dBm, oP_{1dB} is 15.5 dBm, peak PAE is 35.3%, PAE at 1-dB compression is 31.5%, and PAE at 6-dB backoff is 11.5%. Compared with simulations, measurement results show the same P_{sat}, three point lower PAE and 1.5-dB lower oP_{1dB}.

To further assess linearity of the PA, we first measure AM–PM distortion and IM3. The AM–PM distortion measurement shown in Fig. 18 reveals less than 2° up to 1-dB compression point. The swept-power IM3 measurement is presented in Fig. 19. The measured IM3 product at 6-dB backoff with a second tone at 17-, 107-, and 211-MHz offsets from 28 GHz were −34.6, −33.7, and −44 dBc, respectively. Measurements with modulated waveforms are not possible due to equipment limitations; however, our commercial partner did measure our PA and reported error-vector magnitude (EVM) results for a slightly different, and more linear (larger

conduction angle) bias condition in [36]. The measured EVM in this condition was −22 dB at 6-dB backoff for an 800-MHz OFDM signal with 16-level quadrature amplitude modulation. Measured peak PAE was 35% and gain was ~17.3 dB.

Tables II and III summarize the performance of the PA across 27–29 GHz and across temperature. The gain P_{sat} and oP_{1dB} show small variation across the frequency band.

VI. CONCLUSION

We have presented a design methodology to realize a harmonic matching network for PAs operating in the continuous Class-AB mode. The harmonic matching network comprises a Chebyshev bandpass filter cascaded with or subsumed within a fundamental-frequency matching network. This harmonic network is capable of realizing a broad range of fundamental and second-harmonic impedances. When this network is realized with on-chip passive components, the parasitics require some modification to the topology which can be achieved primarily through Norton transformation. Through simulations, we have
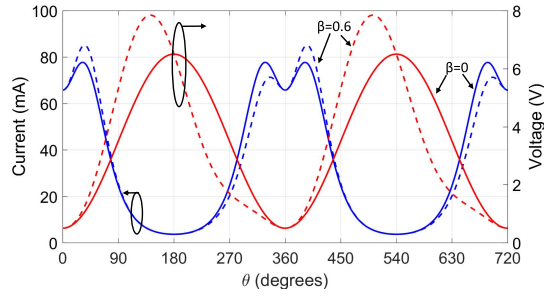
Class	Fundamental Current (mA)	DC current (mA)	Fundamental Voltage (V)	RF power (mW)	DC power (mW)	Drain efficiency (%)
Class AB	39.3	34.7	3	58.9	121.3	48.6
Continuous Class-AB	39∠7°	33.8	3.5∠31°	62.2	118.2	52.7

Fig. 20. Current–voltage waveforms, fundamental and dc components of current and performance metrics to demonstrate the impact of I–V knee on the performance of continuous Class-AB mode ($\beta = 0.6$) and Class-AB mode ($\beta = 0$) at 1-dB compression.

demonstrated that the harmonic termination in continuous Class-AB mode improves PAE at oP$_{1\text{dB}}$ by 4% to 7% points compared with a traditional Class-AB PA as well as a PA realized using a simple LC matching network targeting a fundamental-frequency match only. At 6-dB backoff, the PAE improvement is reduced to around 1% point. The net result is that the PAE can be improved over the range from 6-dB backoff up through oP$_{1\text{dB}}$, reducing power consumption in the transmitter.

We demonstrated the application of this design methodology with a 28-GHz PA designed in a 130-nm SiGe BiCMOS technology. A performance comparison with state-of-the-art PAs in Ka-band and Q-band is shown in Table IV. The PA achieves high peak and backoff PAEs with consistent performance across 27–29 GHz and excellent backoff linearity.

APPENDIX

It has been shown in [6, Ch. 8, pp. 204–216] and [29] that device nonlinearities, especially, the I–V knee and the variable collector capacitance can be used to reduce the overlap between the current and voltage waveforms and the power factor between the fundamental components of voltage and current in second-harmonic tuned PAs. The impact of the nonlinear collector capacitance was presented in [29] which demonstrated that the efficiency and output power of a Class-J PA exceeds that of a Class-B PA near saturation. Here, we show that the I–V knee can also be leveraged to achieve higher output power and efficiency in continuous Class-AB mode, especially, at power levels approaching 1-dB compression.

To incorporate the effect of the I–V knee, the following current waveform, given in [6, Ch. 3, pp. 55–59], is used:

$$I(t) = I_{\max} e^{k(V_q + V_s \cos(\omega t) - 1)}(1 - e^{-V(t)/V_K}) \qquad (24)$$

where $I_{\max}$ is the maximum collector current, V_q is the quiescent input voltage, V_s is the input signal voltage, k is a parameter that determines the sharpness of the device turn-ON characteristic, and $V(t)$ is the collector voltage given by (3).

The I–V waveforms of the continuous Class-AB mode PA and the classical Class-AB PA generated using (3) and (24) near 1-dB compression are shown in Fig. 20. The harmonic components of the current waveform calculated using a Fourier series along with power and efficiency metrics are also shown.

We first observe that for the continuous Class-AB mode ($\beta = 0.6$), the current waveform is asymmetric and has lower overlap with the voltage waveform compared with the classical Class-AB mode ($\beta = 0$). Furthermore, the calculated fundamental current indicates that the power factor is improved compared with the ideal continuous-mode theory, resulting in higher output power and efficiency. Note that the improvement in output power and efficiency of the continuous Class-AB mode over the classical Class-AB mode calculated from the waveforms is somewhat lower than what we demonstrated with simulations in Section IV. This is because we have included only the I–V knee nonlinearity in this analysis, whereas in simulations other nonlinear effects are also accounted for in the device model. Since the effect of the I–V knee (and other nonlinearities) is more pronounced, the continuous Class-AB mode shows a higher performance benefit over the classical Class-AB mode near 1-dB compression compared to backoff power levels as demonstrated in Section IV.

ACKNOWLEDGMENT

REFERENCES

[1] Z. Pi and F. Khan, "An introduction to millimeter-wave mobile broadband systems," *IEEE Commun. Mag.*, vol. 49, no. 6, pp. 101–107, Jun. 2011.

[2] F. Khan, Z. Pi, and S. Rajagopal, "Millimeter-wave mobile broadband with large scale spatial processing for 5G mobile communication," in *Proc. 50th Annu. Allerton Conf. Commun. Control, Comput. (Allerton)*, Oct. 2012, pp. 1517–1523.

[3] T. S. Rappaport *et al.*, "Millimeter wave mobile communications for 5G cellular: It will work!" *IEEE Access*, vol. 1, pp. 335–349, May 2013.

[4] S. C. Thompson, "Constant envelope OFDM phase modulation," Ph.D. dissertation, Dept. Elect. Eng., Univ. California, La Jolla, CA, USA, Jan. 2005.

[5] T. Jiang and Y. Wu, "An overview: Peak-to-average power ratio reduction techniques for OFDM signals," *IEEE Trans. Broadcast.*, vol. 54, no. 2, pp. 257–268, Jun. 2008.

[6] S. C. Cripps, *RF Power Amplifiers for Wireless Communications*, 2nd ed. Norwood, MA, USA: Artech House, 2006.

[7] A. Agah, B. Hanafi, H. Dabag, P. Asbeck, L. Larson, and J. Buckwalter, "A 45GHz Doherty power amplifier with 23% PAE and 18dBm output power, in 45nm SOI CMOS," in *IEEE Int. Microw. Symp. Dig.*, Jun. 2012, pp. 1–3.

[8] A. Agah, H. Dabag, B. Hanafi, P. Asbeck, L. Larson, and J. Buckwalter, "A 34% PAE, 18.6dBm 42–45GHz stacked power amplifier in 45nm SOI CMOS," in *Proc. IEEE RF Integr. Circuits Symp.*, Jun. 2012, pp. 57–60.

[9] K. Datta, J. Roderick, and H. Hashemi, "Analysis, design and implementation of mm-Wave SiGe stacked class-E power amplifiers," in *Proc. IEEE Radio Freq. Integr. Circuits Symp. (RFIC)*, Jun. 2013, pp. 275–278.

[10] N. Kalantari and J. F. Buckwalter, "A 19.4 dBm, Q-band class-E power amplifier in a 0.12 μm SiGe BiCMOS process," *IEEE Microw. Compon. Lett.*, vol. 20, no. 5, pp. 283–285, May 2010.

[11] J.-H. Chen, S. R. Helmi, and S. Mohammadi, "A fully-integrated Ka-band stacked power amplifier in 45nm CMOS SOI technology," in *Proc. IEEE Topical Meeting Silicon Monolithic Integr. Circuits RF Syst.*, Jan. 2013, pp. 75–77.

[12] K. Kal, J. Roderick, and H. Hashemi, "A 20 dBm Q-band SiGe class-E power amplifier with 31% peak PAE," in *Proc. IEEE Custom Integr. Circuits Conf.*, Sep. 2012, pp. 1–4.

[13] W. Tai, L. Carley, and D. Ricketts, "A Q-band SiGe power amplifier with 17.5 dBm saturated output power and 26% peak PAE," in *Proc. IEEE Bipolar/BiCMOS Circuits Technol. Meeting*, Oct. 2011, pp. 146–149.

[14] A. Chakrabarti, J. Sharma, and H. Krishnaswamy, "Dual-output stacked class-EE power amplifiers in 45nm SOI CMOS for Q-band applications," in *Proc. IEEE Compound Semiconductor Integr. Circuit Symp.*, Oct. 2012, pp. 1–4.

[15] H. Dabag, B. Hanafi, F. Golcuk, A. Agah, J. F. Buckwalter, and P. M. Asbeck, "Analysis and design of stacked-FET millimeter-wave power amplifiers," *IEEE Trans. Microw. Theory Techn.*, vol. 61, no. 4, pp. 1543–1556, Apr. 2013.

[16] J. Kim, H. Dabag, P. Asbeck, and J. Buckwalter, "Q-band and W-band power amplifiers in 45-nm CMOS SOI," *IEEE Trans. Microw. Theory Techn.*, vol. 60, no. 6, pp. 1870–1877, Jun. 2012.

[17] S. Y. Mortazavi and K. J. Koh, "A class F-1/F 24-to-31GHz power amplifier with 40.7% peak PAE, 15dBm OP1dB, and 50mW Psat in $0.13\mu m$ SiGe BiCMOS," in *IEEE Int. Solid-State Circuits Conf. Dig. Tech. Papers*, Feb. 2014, pp. 254–255.

[18] S. Y. Mortazavi and K. J. Koh, "A 28-GHz inverse class-F power amplifier with coupled-inductor based harmonic impedance modulator," in *Proc. IEEE Custom Integr. Circuits Conf.*, Sep. 2015, pp. 1–4.

[19] S. Y. Mortazavi and K. J. Koh, "A 38 GHz inverse class-F power amplifier with 38.5% peak PAE, 16.5 dB gain, and 50 mW Psat in 0.13-μm SiGe BiCMOS," in *Proc. IEEE Radio Freq. Integr. Circuits Symp. (RFIC)*, May 2015, pp. 211–214.

[20] J. Essing, D. Leenaerts, and R. Mahmoudi, "A 27GHz, 31 dBm power amplifier in a 0.25 μm SiGe:C BiCMOS technology," in *Proc. IEEE Bipolar/BiCMOS Circuits Technol. Meeting*, Sep. 2014, pp. 143–146.

[21] P. Tasker, V. Carrubba, P. Wright, J. Lees, J. Benedikt, and S. Cripps, "Wideband PA design: The 'Continuous' mode of operation," in *Proc. IEEE Compound Semiconductor Integr. Circuit Symp.*, Oct. 2012, pp. 1–4.

[22] T. Canning, P. J. Tasker, and S. C. Cripps, "Continuous mode power amplifier design using harmonic clipping contours: Theory and practice," *IEEE Trans. Microw. Theory Techn.*, vol. 62, no. 1, pp. 100–110, Jan. 2014.

[23] S. Rezaei, L. Belostotski, F. M. Ghannouchi, and P. Aflaki, "Integrated design of a class-J power amplifier," *IEEE Trans. Microw. Theory Techn.*, vol. 61, no. 4, pp. 1639–1648, Apr. 2013.

[24] P. Wright, J. Lees, J. Benedikt, P. J. Tasker, and S. C. Cripps, "A methodology for realizing high efficiency class-J in a linear and broadband PA," *IEEE Trans. Microw. Theory Techn.*, vol. 57, no. 12, pp. 3196–3204, Dec. 2009.

[25] N. Tuffy, A. Zhu, and T. J. Brazil, "Class-J RF power amplifier with wideband harmonic suppression," in *IEEE Int. Microw. Symp. Dig.*, Jun. 2011, pp. 1–4.

[26] V. Carrubba et al., "Exploring the design space for broadband pas using the novel 'continuous inverse class-F mode,'" in *Proc. 41st Eur. Microw. Conf. (EuMC)*, Oct. 2011, pp. 333–336.

[27] A. Sarkar and B. Floyd, "A 28-GHz class-J power amplifier with 18-dBm output power and 35% peak PAE in 120-nm SiGe BiCMOS," in *Proc. IEEE Topical Meeting Silicon Monolithic Integr. Circuits RF Syst.*, Jan. 2014, pp. 71–73.

[28] Y. Chen, H. Shen, and X. Liu, "A new layout method to improve the thermal stability of multi-finger power HBT," in *Proc. IEEE Int. Conf. (ASIC)*, Oct. 2009, pp. 344–346.

[29] J. Moon, J. Kim, and B. Kim, "Investigation of a class-J power amplifier with a nonlinear C_{out} for optimized operation," *IEEE Trans. Microw. Theory Techn.*, vol. 58, no. 11, pp. 2800–2811, Nov. 2010.

[30] K. Mimis, K. A. Morris, S. Bensmida, and J. P. McGeehan, "Multichannel and wideband power amplifier design methodology for 4G communication systems based on hybrid class-J operation," *IEEE Trans. Microw. Theory Techn.*, vol. 60, no. 8, pp. 2562–2570, Aug. 2012.

[31] M. B. Steer, *Microwave and RF Design: A Systems Approach*. Raleigh, NC, USA: SciTech Pub., 2010.

[32] R. M. Fano, "Theoretical limitations on the broadband matching of arbitrary impedances," Ph.D. dissertation, Dept. Elect. Eng. Comput. Sci., Massachusetts Inst. Technol., Cambridge, MA, USA, Jan. 1948.

[33] I. Hunter, *Theory and Design of Microwave Filters*. London, U.K.: IEE, 2001.

[34] *BiCMOS-8HP Model Reference Guide, V1.6.0.0*, VT, USA: IBM, 2014.

[35] H. T. Dabag, J. Kim, L. E. Larson, J. F. Buckwalter, and P. M. Asbeck, "A 45-GHz SiGe HBT amplifier at greater than 25% efficiency and 30 mW output power," in *Proc. IEEE Bipolar/BiCMOS Circuits Technol. Meeting*, Oct. 2011, pp. 25–28.

[36] F. Aryanfar, "Enabling mobile communication at mm-wave using phased arrays," in *Proc. IEEE RF Integr. Circuits Symp., Workshop Adv. SiGe CMOS Phased Array Syst. 3 to 100 GHz (WSG)*, Jun. 2014.

[37] W. Tai, L. R. Carley, and D. S. Ricketts, "A 0.7W fully integrated 42GHz power amplifier with 10% PAE in 130nm SiGe BiCMOS," in *IEEE Int. Solid-State Circuits Conf. Dig. Tech. Papers*, Feb. 2013, pp. 142–143.

[38] R. Bhat, A. Chakrabarti, and H. Krishnaswamy, "Large-scale power-combining and linearization in watt-class mmwave CMOS power amplifiers," in *Proc. Radio Freq. Integr. Circuits Symp. (RFIC)*, Jun. 2013, pp. 283–286.

[39] K. Datta and H. Hashemi, "2.9 A 29dBm 18.5% peak PAE mm-wave digital power amplifier with dynamic load modulation," in *IEEE Int. Solid-State Circuits Conf. (ISSCC) Dig. Tech. Papers*, Feb. 2015, pp. 1–3.

[40] A. Chakrabarti and H. Krishnaswamy, "High-power high-efficiency class-E-like stacked mmwave PAs in SOI and bulk CMOS: Theory and implementation," *IEEE Trans. Microw. Theory Techn.*, vol. 62, no. 8, pp. 1686–1704, Aug. 2014.

Anirban Sarkar (S'10) received the B.E. degree in electrical engineering from the National Institute of Technology, Durgapur, India, and the M.S. and Ph.D. degrees in electrical engineering from North Carolina State University, Raleigh, NC, USA, in 2011 and 2016, respectively.

In 2015, he was an Intern with Samsung Research America, Dallas, TX, USA. His current research interests include RF and millimeter-wave integrated circuits, especially, linear and power-efficient transmitters and power amplifiers.

Dr. Sarkar has served as a reviewer for the IEEE JOURNAL OF SOLID-STATE CIRCUITS.

Brian A. Floyd (S'98–M'01–SM'10) received the B.S. (with highest distinction), M.Eng., and Ph.D. degrees in electrical and computer engineering from the University of Florida, Gainesville, FL, USA, in 1996, 1998, and 2001, respectively.

He held the Intersil/Semiconductor Research Corporation Fellowship and the Pittman Fellowship at the University of Florida, where he was involved in CMOS RFIC design for on-chip wireless clock distribution. In 2001, he became a Research Staff Member at the IBM Thomas J. Watson Research Center, Yorktown Heights, NY, USA, where he was involved in the development of 3G WCDMA receivers in SiGe BiCMOS and CMOS technologies and then the investigation and demonstration of some of the first silicon-based millimeter-wave receivers, transmitters, and frequency synthesizers for applications at 60 GHz and above. In 2007, he became the Manager of the Wireless Circuits and Systems Group at IBM Research, Yorktown Heights, NY, USA, leading the development of 60-GHz phased-array transceiver, antenna, and package solutions under IBM and the MediaTek joint development program. In 2010, he joined the Department of Electrical and Computer Engineering, North Carolina State University, Raleigh, NC, USA, as an Associate Professor. He has authored or coauthored over 84 technical papers and holds 22 issued patents. His current research interests include RF and millimeter-wave circuits and systems for communications, radar, and imaging applications.

Dr. Floyd was a recipient of the 2016 NC State Outstanding Teacher Award, the 2015 NC State Chancellors Innovation Award, the 2014 IBM Faculty Award, the 2011 DARPA Young Faculty Award, the 2004 and 2006 IEEE Lewis Winner Awards for best paper at the International Solid-State Circuits Conference (ISSCC), and the 2006 and 2011 Pat Goldberg Memorial Awards for the best paper within IBM Research. He is an Associate Editor of the IEEE JOURNAL OF SOLID-STATE CIRCUITS and has served on the Technical Program Committee for ISSCC. He currently serves on both the Steering and Technical Program Committees for the RFIC Symposium. From 2006 to 2009, he served on the Technical Advisory Board to the Semiconductor Research Corporation (SRC) integrated circuits and systems science area, and currently serves as a Thrust Leader for the SRCs Texas Analog Center of Excellence.